Microscopy and Microanalysis, 2024, **00**, 1–14
https://doi.org/10.1093/mam/ozae124

Original Article

Microscopy AND Microanalysis

Estimation of Dislocation Densities With Nondestructive Scanning Electron Microscope Techniques: Application to Gallium Nitride

Arka Mandal[1], Benoît Beausir[1], Julien Guyon[1], Vincent Taupin[1], and Antoine Guitton[1,*]

[1]*Université de Lorraine, CNRS, Arts et Métiers, LEM3, Metz 57070, France*

***Corresponding author:** Antoine Guitton, E-mail: antoine.guitton@univ-lorraine.fr

Abstract

Characterizing threading dislocations (TDs) in gallium nitride (GaN) semiconductors is crucial for ensuring the reliability of semiconductor devices. The current research addresses this issue by combining two techniques using a scanning electron microscope, namely electron channeling contrast imaging (ECCI) and high-resolution electron backscattered diffraction (HR-EBSD). It is a comparative study of these techniques to underscore how they perform in the evaluation of TD densities in GaN epitaxial layers. Experiments reveal that the dislocation line vectors mostly deviate from the growth direction of the film, i.e., ∦ [0001], followed by edge-type dislocations (dislocation lines ∥ [0001]) with insignificant screw character. Furthermore, TDs from the dislocation clusters are characterized as edge- and (edge + mixed)-type TDs. By combining ECCI counting of dislocations and HR-EBSD description of geometrically necessary dislocation density type, it is possible to measure the total TD density and provide the proportion of pure (edge and screw) and mixed TDs. It has also been observed from the analyses of residual elastic strain fields and lattice rotations that it is not possible to identify individual dislocations for the spatial resolution of 50 nm in HR-EBSD. Nevertheless, ECCI and HR-EBSD can be complementarily used to count and characterize the TDs.

Key words: ECCI, GaN, GND, HR-EBSD, threading dislocation

Introduction

Since its inception in the early 90 s, gallium nitride (GaN) has been considered a modern-age III–V semiconductor material owing to its favorable material parameters, such as wider band gap, higher electron mobility, and electron saturation velocity than that of its counterpart, Si. These properties make GaN suitable for high-frequency and high-power devices (Vetury et al., 2001; Kikkawa et al., 2009; Runton et al., 2013; Kaminski & Hilt, 2014). Although, GaN is vastly being exploited more and more in diverse fields of application, such as automotive (electric and fuel cell vehicles; Kachi, 2018; Groon et al., 2023), industrial (5G, wireless sensor networks, and internet of things; Xu et al., 2023), data center (cloud computing; Forouzesh et al., 2020), aerospace and defense (microwave, mixed signal, and optoelectronic products; Streit et al., 2005), consumer electronics (wireless chargers and ultra-thin power adapters; Pushpakaran et al., 2020), wireless communication (Ohno & Kuzuhara, 2001), medical technology (biomedical implant; Mishra et al., 2023), etc., it is already established to be a game changer for high-efficiency power transistors and integrated circuits in particular (Tanaka et al., 2010; Nikandish, 2023).

The major difficulty in attaining large single crystals of GaN is its high melting point and large dissociation pressure. Hence, GaN film has to be deposited by some vapor deposition method on a substrate (e.g., sapphire, silicon, or silicon carbide) having similar lattice constants and thermal expansion coefficient, following a heteroepitaxial growth (Kwong et al., 2011). Depending on the differences between these quantities with that of the substrate, GaN tends to experience compressive/tensional biaxial strain (Pearton, 2021). This strain in the epilayer is released by the formation of threading dislocations (TDs), originating from the substrate and thin film GaN interface (nucleation layer) itself (Kapolnek et al., 1995). TDs can be <a>-type ($\boldsymbol{b} = 1/3 \langle 11\bar{2}0 \rangle$), i.e., edge (prismatic), or <a + c>-type ($\boldsymbol{b} = 1/3 \langle 11\bar{2}3 \rangle$), i.e., mixed, or <c>-type ($\boldsymbol{b} = \langle 0001 \rangle$), i.e., screw, and the dislocation line direction is either parallel to [0001], i.e., the growth direction (for edge and screw TDs; Moram et al., 2009) or at about 12° to it (for mixed TDs; Mathis et al., 2000). Edge TDs are likely to be initiated during adjacent island coalescence, producing subgrains that are tilted or twisted (which requires screw TDs as well) to each other. This is commonly known as the "mosaic" model (Wu et al., 1998). Contrarily, the "nucleation layer model" tells that TDs start appearing in the initially annealed low-temperature nucleation layer and eventually extend (but not along the coalescence boundaries) as the film grows (Narayanan et al., 2001). The generation of screw or mixed TDs is found to be more complex, and their density decreases as the film thickness increases, owing to the ease of cross slip (Kapolnek et al., 1995). There are reports claiming that the dislocation density (DD) reduces by the formation of half-loops, as the GaN film thickness increases (Chien et al., 1996; Lee & Auh, 2001). Although TDs are formed to relieve the lattice misfit strain (Wang, 2012), these cannot completely be removed (Smalc-Koziorowska et al., 2020).

Generally, TDs, being the nonradiative recombination centers, degrade the emission intensity (Choi et al., 2004). Furthermore, TDs, particularly screw-type, may detrimentally

Received: July 26, 2024. **Revised:** October 24, 2024. **Accepted:** November 25, 2024

influence the leakage current also (Usami et al., 2018). Therefore, it is crucial to identify and characterize them to ensure the end physical properties. The dislocation densities can be categorized as statistically stored (SSD density), i.e., related to plastic strain but with null overall Burgers vector, or geometrically necessary (GND density), i.e., associated with strain gradients and nonzero overall Burgers vector (Voyiadjis & Peters, 2010). The total DD combines both of these, and the proportion of GND density depends on the scale of observation. In this regard, high-resolution electron backscattered diffraction (HR-EBSD) has been proven to produce high-accuracy data with angular resolution in the limit of about 0.01° (Vilalta-Clemente et al., 2015), which can be used to estimate the GND density measured from the lattice curvature on the surface (Wilkinson & Randman, 2010). However, depending upon various factors, such as scanning step size, interspacing, and type of TDs (SSDs or GNDs) present, HR-EBSD may give rise to results with missing information. In this context, if the interspacing between two adjacent dislocations is less than the chosen step size or there is a cluster of dislocations producing a null net Burgers vector, HR-EBSD is likely to underestimate the counts of dislocations (Jiang et al., 2013). Within this framework, another nondestructive characterization technique, i.e., electron channeling contrast imaging (ECCI), has emerged, which can efficiently be used for fast identification of all types of TDs (Naresh-Kumar et al., 2012; Zaefferer & Elhami, 2014; Dunlap et al., 2018; Kriaa et al., 2017, 2019, 2021; Picard et al., 2007; Vilalta-Clemente et al., 2017) by using the concept of channeling, varying the backscattering yield. A study on InAlN semiconductors grown on SiC and sapphire substrates combining these techniques is effective for the quantitative measurements of structural defects (Vilalta-Clemente et al., 2017). However, the step size for HR-EBSD used in this study was quite large, i.e., 200 nm, as it is anticipated that a reduction in the step size may increase the noise floor, causing a misinterpretation of the GND density (Jiang et al., 2013). Nevertheless, GaN semiconductor, which is expected to exhibit a higher order DD (Amano et al., 1986), has not been examined so far using these two methods complementarily, with a high spatial resolution of HR-EBSD in the limit of a single dislocation. A recent article has dealt with both these techniques for characterizing GaN thin film on GaN substrate. Still, it is more of a comparative study between these two techniques where the region of interest and the EBSD step size were quite larger than the present work (Ruggles et al., 2021). Some cross-correlation–based HR-EBSD and ECCI studies demonstrated strain mapping and dislocation distributions; however, the EBSD step size used was about three to four times than what it is in the present work (Vilalta-Clemente et al., 2017; Naresh-Kumar et al., 2022).

The present study aims to identify the TDs from ECCI observations and measure the total DD by this nondestructive SEM technique with a high spatial resolution and accuracy and also carry out various analyses using HR-EBSD to study the characteristics of the same. We show that, by combining ECCI counting of dislocations and HR-EBSD description of GND density type, it is possible to measure the total TD density and provide the proportion of pure (edge and screw) or mixed TDs in GaN thin film semiconductor. This will broadly help the semiconductor industry to develop the state-of-the-art in quick and quantitative assessment of structural defects, i.e., TDs.

Materials and Methods

Sample Specifics

The GaN thin film studied in this work has been grown by metal-organic chemical vapor deposition (MOCVD) technology on [111]-oriented Si substrate (Zhu et al., 2013; Zhong et al., 2022). The topmost layer is carbon-doped GaN (GaN:C), having a thickness of about 80 nm, followed by a silicon-doped nGaN layer of 1.7 μm thickness. In between the nGaN layer and the Si substrate, there is a buffer stack of around 1 μm thickness, composed of various layers, which is usual in GaN-on-Si heteroepitaxy. It is introduced as a strain engineering stack to adapt the lattice and thermal expansion mismatches between GaN and Si. Sparsely placed thin gold contacts on top of the film are not relevant to this work. The top surface (in the large areas between the contacts) is thus [0001]-oriented GaN:C, which is investigated using different techniques.

Electron Channeling Contrast Imaging

ECCI uses the principle of channeling backscattered electrons and variation of its yield as a function of the orientation of the incident beam with respect to the lattice planes (Booker et al., 1967; Coates, 1967). The circular, electron-sensitive detector is placed usually just below the polar piece to collect only those electrons with a deflection angle >90°. The imaging is done with an electron beam energy and current of 20 keV and ≈5.5 nA, respectively, at a working distance of 9.2 mm and a specimen tilt of 7.8° to achieve the perfect channeling contrast inside a Dual Beam FIB-SEM Zeiss® Auriga 40 scanning electron microscope (SEM). The pixel size in the electron channeling contrast (ECC) micrograph is 3.278 nm, the beam dwell time is 76.2 μs, and the image is captured as a single frame. Each line is averaged over six scans (the dwell time for each line per scan is 12.7 μs). The lowest backscattering yield has been attained at the edge of $(11\bar{2}0)$ band, as identified by the electron channeling pattern (ECP), for the best contrast. Notably, this is a direct measurement technique for the dislocations.

High-Resolution Electron Backscattered Diffraction

HR-EBSD experiment is carried out at 70° tilt toward the detector to optimize the convenience of experimentation and pattern contrast all together. Typically, a phosphor screen is used as the detector that captures the electrons backscattered inelastically from the sample surface, giving rise to a diffraction pattern, i.e., electron backscattering pattern (EBSP). A digital camera finally obtains the image of the EBSP. No background correction is performed by removing the recorded image before the HR-EBSD analysis, and only a high-pass log filter is applied on the raw patterns. HR-EBSD offers substantially higher angular resolution, when compared with conventional EBSD, aiding in measuring $\sim 1 \times 10^{-4}$ rad of relative disorientation (Wilkinson et al., 2006). The EBSP images are averaged by three to enhance the signal-to-noise ratio. An area of size $3.2 \times 3.0\ \mu m^2$ (64×60 pixels) is scanned under HR-EBSD with an acceleration voltage of 20 kV, probe current of 5 nA, a step size of 50 nm, and a 100% index rate. A total of 3,840 patterns are captured and recorded for the map at the full resolution of the HR-EBSD symmetry camera (Oxford). The experiment is performed inside FIB-SEM Zeiss® Auriga, fitted with an EBSD system, and the results are analyzed using

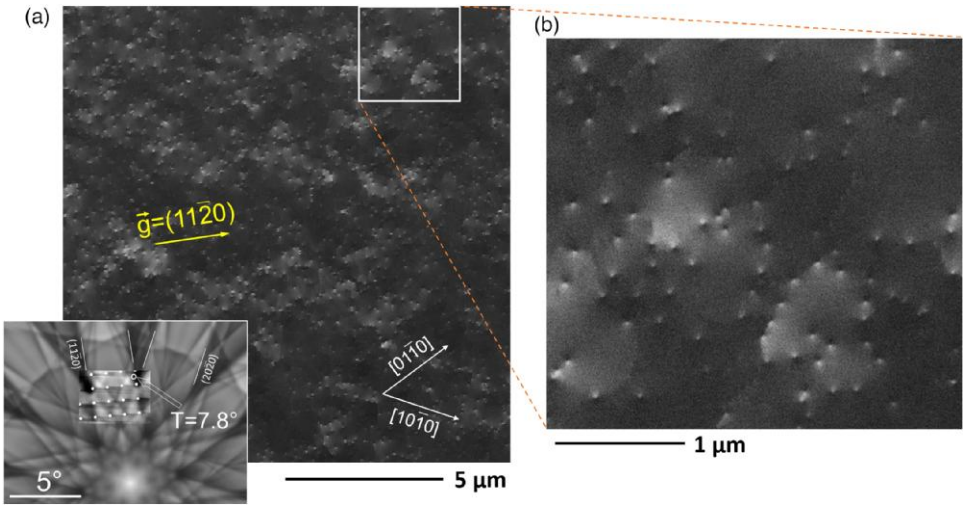

Fig. 1. ECC micrograph of (0001) GaN surface showing the TDs appearing either brighter or revealing black and white contrast on a darker background. The magnified image of the region inside the white-bordered rectangle within (**a**) is displayed in (**b**). The inset within (**a**) shows the ECP superimposed on an EBSD pattern simulated for a 5° tilt where the area shown in the ECC micrograph is taken from the circled region at a tilt of 7.8° for perfect channeling.

Analysis Tools for Electron and X-ray diffraction (ATEX©) software (Beausir & Fundenberger, 2017). No smoothing is performed on the HR-EBSD results. The sample is oriented in such a way that the [0001] direction is pointed out of the sample surface plane. Unlike ECCI, HR-EBSD is an indirect method to characterize the dislocations.

Results and Discussion

Observation by ECCI

Since GaN is a large single crystal, ECPs can be useful to ensure that the perfect channeling condition is met just by placing the edge of a certain channeling band along the optic axis of the microscope (Booker et al., 1967; Ayers & Joy, 1972; Kriaa et al., 2017). One such pattern is displayed in Figure 1a (inset), superimposed on a reference pattern simulated by ESPRIT DynamicS 1.0 by Bruker. The pattern is simulated at 5° because in ECCI the specimen is placed at a tilt angle close to this, i.e., 7.8°. The rectangular area of size 9.6 μm^2, marked within the ECC micrograph captured on [0001] plane (Fig. 1a), is taken into consideration for the dislocation analysis further. TDs, i.e., dislocations nearly perpendicular to the observation surface, appear as spots with dark and bright contrast as shown in Figure 1. The total number of dislocations identified and counted manually within this region is 139 (Fig. 1b). From this observation following the ECCI method, the total DD is calculated to be $\sim 1.4 \pm 0.14 \times 10^9$ cm^{-2}.[1] The DD (ρ) has been estimated by calculating N_{tot}/A, where N_{tot} is the total number of dislocations within the area A (in cm^2). The major advantage of determining the total DD using the ECCI method is that it is likely to characterize all the surface penetrating TDs within the area of interest under all diffraction conditions attributed to the surface relaxation. This makes the analysis more reliable and statistically significant over other techniques where some TDs can be left undetected. Importantly, in ECCI, TDs do not go out of contrast under different channeling conditions unlike inclined dislocations (Kriaa et al., 2017, 2019), which allows a better estimation of the DD (Vilalta-Clemente et al., 2017; Habiyaremye et al., 2021, 2024). However, with a single diffraction condition, i.e., using a particular **g**-vector that is (11$\bar{2}$0) in the present study, it is not plausible to readily distinguish between the types of dislocations, i.e., screw or edge, using this method. Even if the diffraction conditions are unidentified, it is possible to characterize the pure edge dislocations and dislocations with screw component by comparing the directions of black and white "butterfly" contrast patterns of TDs between two ECC micrographs captured using two different **g**-vectors (that are at 120° to each other) from a particular region of the sample (Naresh-Kumar et al., 2012). Nevertheless, this approach is not undertaken in the present work.

Observation by HR-EBSD

The identical region of interest studied by the ECCI method has been taken into consideration for further investigation under HR-EBSD. Importantly, HR-EBSD is sensitive to only 5–10 nm depth from the top surface (this depth is subjected to change depending on electron acceleration voltage, atomic number of the material, etc.) and, consequently, does not tend to detect subsurface defects other than TDs penetrating the surface, which makes the comparison between HR-EBSD and ECCI reasonable in terms of density determination of TDs. The challenging part is to align the images perfectly to obtain the same microstructural area by both techniques, which is attributed to the difference in the sample tilting with respect to the detector and also the drifting during HR-EBSD acquisition. An ImageJ plugin, TrakEM2 (Cardona et al., 2012), is used for image montaging where two different layers (images) are aligned by manually selecting the landmarks (56 points) and finally applying transform with free affine. The ECC micrographs along with the reference virtual forescatter diode image obtained during HR-EBSD acquisition are shown in Figures 2a and 2b, respectively. Here, the position of the TDs (different color than the neighboring pixels) and subgrain boundaries (partitioning two adjacent zones

[1] Uncertainty, $\Delta\rho = \rho[(\Delta N/N_{tot}) + (\Delta l/l) + (\Delta w/w)]$, where, ΔN (≈ 5) is the number of dislocations that may have been missed while counting them, N_{tot} (≈ 139) is the total number of dislocations, $\Delta l = \Delta w$ ($\approx 0.1\,\mu m$), l ($=3\,\mu m$), and w ($=3.2\,\mu m$) are the length and width of the area of interest, respectively.

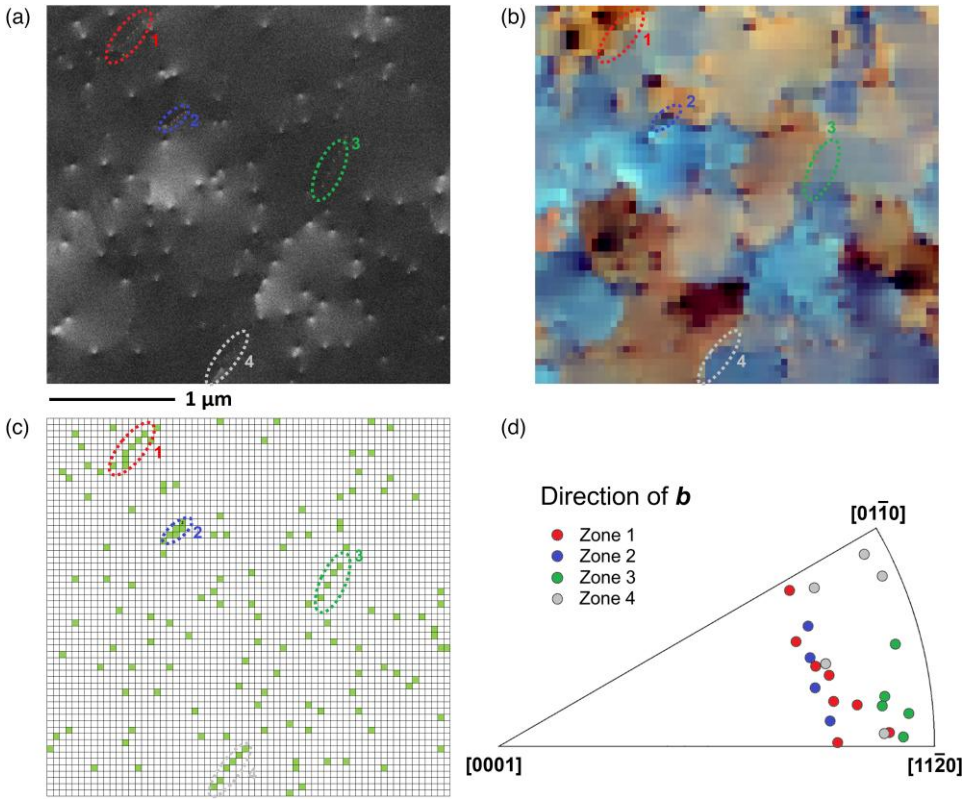

Fig. 2. (**a**) The ECC micrograph of the area of interest where orange dots denote the TDs, (**b**) the reference virtual forescatter diode image obtained during HR-EBSD acquisition, which is utilized to transform the ECC micrograph, (**c**) the 60 × 64 grids ($l \times w$) display, with each grid having the same size as the size of the pixel used in HR-EBSD, showing the exact positions of the TDs observed using ECCI, and (**d**) the direction of Burgers vectors of the TDs from different dislocation clusters (zones) shown in (**a**–**c**).

with different colors) can be compared between these two images. To specifically locate the dislocations, as identified by the ECCI method (Fig. 2a), the area of interest has been divided into a 60×64 grid ($l \times w$), with each cell having the same size as the size of the pixel used in 2D HR-EBSD (Fig. 2c). This gridding method helps facilitate the comparison between the two methods. Dislocation clusters are marked by oval shapes of different colors in the grid map. The distance between two adjacent dislocations is more than the size of the pixel in most of the cases (only one pixel contains two dislocations, as identified by the ECCI method within zone 2 in Fig. 2c). Also, the Burgers vectors of dislocations within clusters (corresponding to different zones as shown in Fig. 2a) are denoted by respective colors in the crystal reference frame (Fig. 2d). The dislocation arrays are mostly dislocation clusters with a similar direction of the Burgers vector and are more of edge-type (or mixed-type with large edge component) dislocations. The minimum deviation of the Burgers vector from the [0001] pole direction, i.e., a pure screw dislocation, is 65.05° (corresponding to zone 1). Notably, it is not possible to distinguish multiple dislocations below the ECCI lateral resolution (which can be as small as 5 nm with a probing depth of around 100 nm), which is not the scenario in this study. Most of the TDs located within the nucleation layer are originated from faulted regions, i.e., those are misfit dislocations (Narayanan et al., 2001). Therefore, TDs are mostly GNDs and not SSDs. Moreover, since each dislocation corresponds to an individual data point, the HR-EBSD treats all the dislocations as GNDs, irrespective of their formation mechanism.

Lattice Rotations

Analysis by HR-EBSD data (based on a user-chosen reference point) is realized to attain the lattice rotation (ω_{ij}) maps. The calculations are done in the framework of finite rotation, assuming traction-free conditions, i.e., σ_{33} is considered zero. Figure 3 shows the maps of computable stress components. The map corresponding to the σ_{33} component displays a negligible near-zero value, which makes the assumption legitimate. The elastic constants used for this calculation are as follows (Polian et al., 1996): $C_{11} = C_{22} = 390$ GPa, $C_{12} = C_{21} = 145$ GPa, $C_{13} = C_{31} = C_{23} = C_{32} = 106$ GPa, $C_{33} = 398$ GPa, $C_{44} = C_{55} = 105$ GPa, and $C_{66} = 123$ GPa.

The sample is oriented in such a way that the [0001] direction is perpendicular to the plane of line scanning and two mutually perpendicular directions, i.e., [74$\bar{1}\bar{1}$0] and [$\bar{5}$6$\bar{1}$0] lie parallel to the x_1 and x_2 direction of the specimen, respectively. It is to be noted that these two directions are 8.9° rotated clockwise about axis [0001] from the conventional [11$\bar{2}$0] and [$\bar{1}$100] directions, respectively. The displacement gradient tensor can be divided into symmetric and antisymmetric components, and the latter can be used to obtain the lattice rotations by the following equation (Asaro, 1979):

$$\omega_{ij} = \frac{1}{2}\left(\frac{\partial u_i}{\partial x_j} - \frac{\partial u_j}{\partial x_i}\right) \quad (1)$$

where x_i is a crystal direction and u_i is the displacement in that direction. ω_{12} is the in-plane rotation, i.e., tilt about surface normal x_3, and ω_{13} and ω_{23} are the out-of-plane rotations, i.e., tilts about x_2 and x_1, respectively.

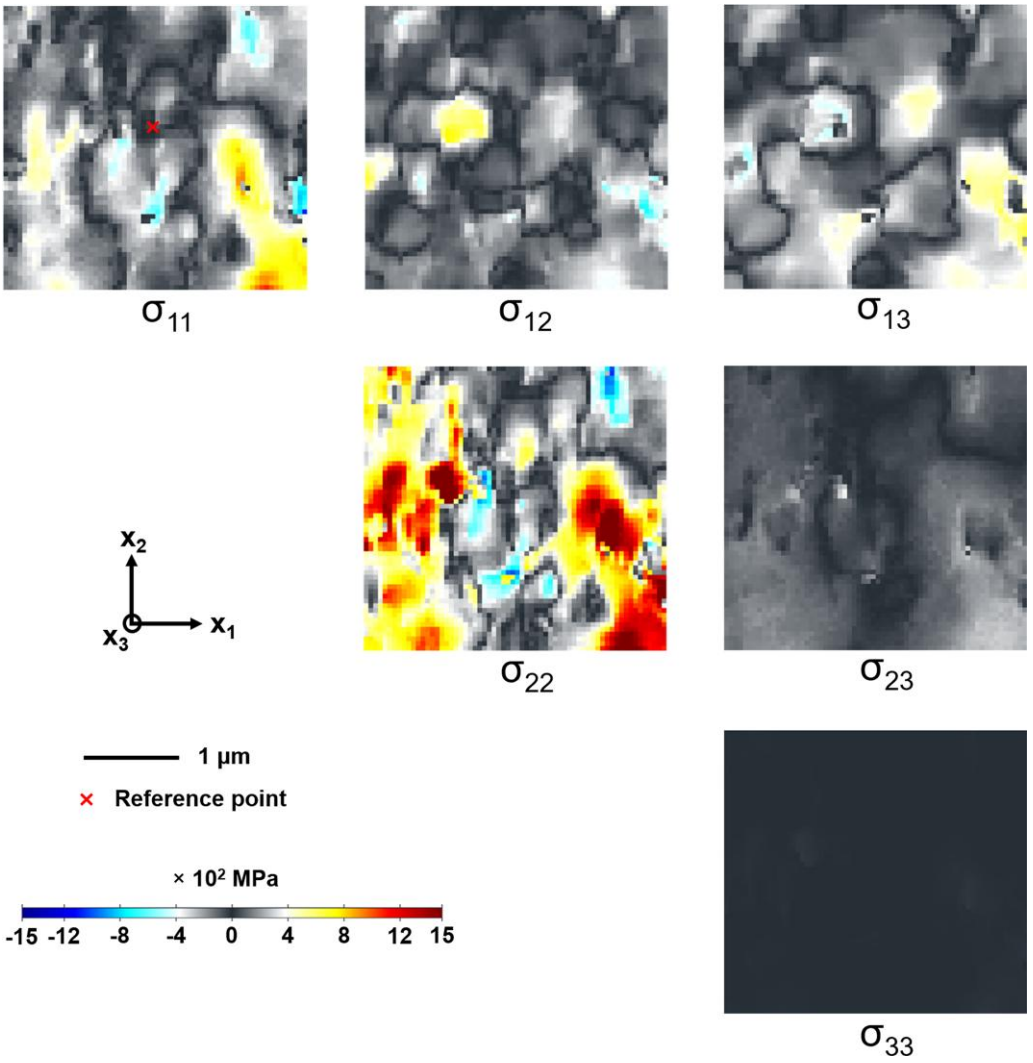

Fig. 3. The stress components calculated from the HR-EBSD data, showing almost no tangential stress, i.e., $\sigma_{33} \approx 0$.

The lattice rotation maps are shown in Figure 4 in the range between −0.25 and +0.25°. The EBSP reference point is a user-chosen option, which is indicated by a red cross within ω_{12}, and lattice rotations are calculated with respect to that point. For correlation, the TDs, as identified by ECCI, are superimposed on the rotation maps (pink dots).

Figure 4 exhibits two out-of-plane lattice rotations, i.e., ω_{23} and ω_{13} about axes $x_1 \parallel [74\bar{1}\bar{1}0]$ and $x_2 \parallel [\bar{5}6\bar{1}0]$, respectively, and one in-plane lattice rotation, i.e., ω_{12} about axis $x_3 \parallel [0001]$. The magnitude of the in-plane tilt rotation is discerned to be appreciably greater than that of the out-of-plane tilt rotations. The distribution of the rotation angles reveals a wider spread for ω_{12} than that of ω_{23} and ω_{13}. Domains of opposite lattice rotations are found adjacent to each other, particularly within ω_{12}. This is indicative of the fact that the number of (edge + mixed)- and edge-type dislocations is greater than the number of screw-type dislocations within the area of interest. Interestingly, the position of the TDs does not exactly match the subgrain boundaries, especially toward the bottom of the maps. Depending on the deviation parameter (which is slightly positive in the present case, i.e., just outside the edge of the band), the center of the black and white contrast does not necessarily coincide with the exact position of the inclined dislocation core (Kriaa et al., 2017, 2019).

Nye's DD Tensor

Nye introduced the DD tensor (α_{ij}) to quantify GND densities (Nye, 1953):

$$\alpha_{ij} = b_i t_j \tag{2}$$

Where b_i is the total length of Burgers vector (of all dislocation lines present) per unit surface, and t_j is the unit dislocation line vector. This yields a signed DD in units of m^{-1}. Dividing this value by the magnitude of the Burgers vector produces a density in units of m^{-2}, which is comparable with conventional dislocation densities. The direction normal to the free surface is the x_3 direction for the present study, $i = 1$ or 2 and $j = 3$ correspond to pure edge dislocations, and $i = j = 3$ to pure screw dislocations, as the dislocation line always goes perpendicular (or nearly) to the film surface irrespective of the type of dislocation (edge or screw).

The Nye's DD tensor, $\boldsymbol{\alpha}$, can also be computed considering the Nye–Kröner theory (Nye, 1953; Kröner, 1959):

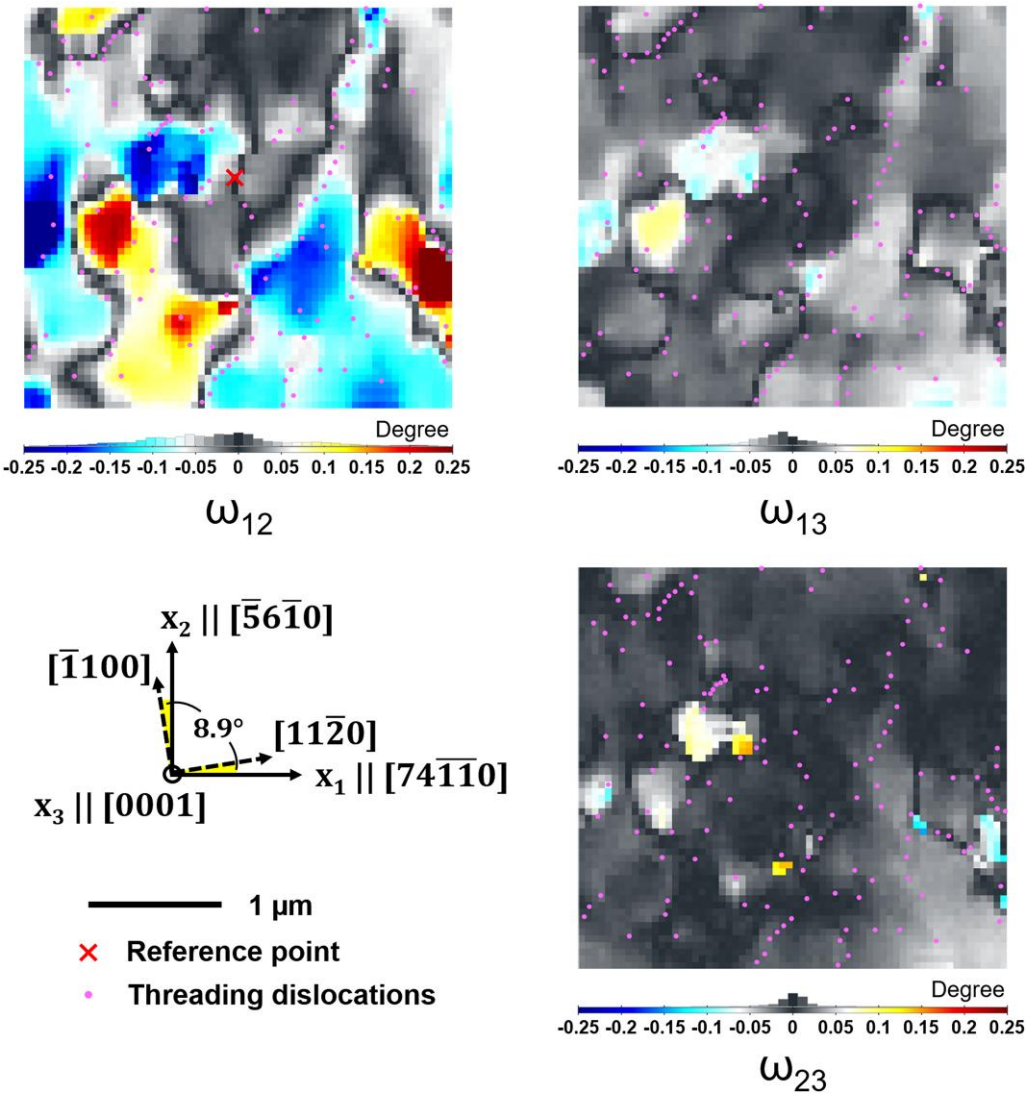

Fig. 4. Lattice rotations with respect to the datapoint shown by the red cross in ω_{12}. The red cross in ω_{12} is the user-chosen EBSP reference point, where the pixels with black, yellow/red, and cyan/blue colors correspond to areas with no rotation, positive rotation, and negative rotation, respectively, corresponding to a tilt about x_3 || [0001]. The sample reference axes are shown in the figure. TDs are superimposed on the maps as pink dots. The same color bar is used for all rotations.

$$\boldsymbol{\alpha} = \mathbf{curl}\ \boldsymbol{\varepsilon} + \mathrm{tr}(\boldsymbol{\kappa_e})\boldsymbol{I} - \boldsymbol{\kappa_e}^{\mathrm{T}} \tag{3}$$

Where $\boldsymbol{\epsilon}$ and $\boldsymbol{\kappa_e}$ are the elastic strain tensor and lattice curvature, respectively. Again, these lattice curvatures can be expressed by a finite difference in rotation term:

$$\kappa_{ij} \cong \frac{\Delta\omega_i}{\Delta x_j} \tag{4}$$

Where $\Delta\omega_i$ is the difference in rotation ω_i (with respect to the reference point on the basis of the sample reference system) between two adjacent pixels spatially separated by Δx_j in the j-th direction. It is to be noted that the GND density obtained by this method is, therefore, a function of the step size used in HR-EBSD (Jiang et al., 2013).

HR-EBSD assumes spatial derivatives along the surface normal direction, i.e., x_3, which are unknown as EBSD takes 2D measurements:

$$\boldsymbol{\alpha} = \begin{bmatrix} \frac{\partial\varepsilon_{12}}{\partial x_3} - \frac{\partial\varepsilon_{13}}{\partial x_2} & \frac{\partial\varepsilon_{13}}{\partial x_1} - \frac{\partial\varepsilon_{11}}{\partial x_3} & \frac{\partial\varepsilon_{11}}{\partial x_2} - \frac{\partial\varepsilon_{12}}{\partial x_1} \\ \frac{\partial\varepsilon_{22}}{\partial x_3} - \frac{\partial\varepsilon_{23}}{\partial x_2} & \frac{\partial\varepsilon_{23}}{\partial x_1} - \frac{\partial\varepsilon_{21}}{\partial x_3} & \frac{\partial\varepsilon_{21}}{\partial x_2} - \frac{\partial\varepsilon_{22}}{\partial x_1} \\ \frac{\partial\varepsilon_{32}}{\partial x_3} - \frac{\partial\varepsilon_{33}}{\partial x_2} & \frac{\partial\varepsilon_{33}}{\partial x_1} - \frac{\partial\varepsilon_{31}}{\partial x_3} & \frac{\partial\varepsilon_{31}}{\partial x_2} - \frac{\partial\varepsilon_{32}}{\partial x_1} \end{bmatrix} + \begin{bmatrix} \frac{\partial\omega_{12}}{\partial x_3} + \frac{\partial\omega_{31}}{\partial x_2} & \frac{\partial\omega_{13}}{\partial x_1} & \frac{\partial\omega_{21}}{\partial x_1} \\ \frac{\partial\omega_{32}}{\partial x_2} & \frac{\partial\omega_{23}}{\partial x_1} + \frac{\partial\omega_{12}}{\partial x_3} & \frac{\partial\omega_{21}}{\partial x_2} \\ \frac{\partial\omega_{32}}{\partial x_3} & \frac{\partial\omega_{13}}{\partial x_3} & \frac{\partial\omega_{31}}{\partial x_2} + \frac{\partial\omega_{23}}{\partial x_1} \end{bmatrix} \tag{5}$$

Here, the α_{i3} components [i.e., α_{13} (edge), α_{23} (edge), and α_{33} (screw)] are completely computable from 2D EBSD data (El-Dasher et al., 2003; Pantleon, 2008) and allow

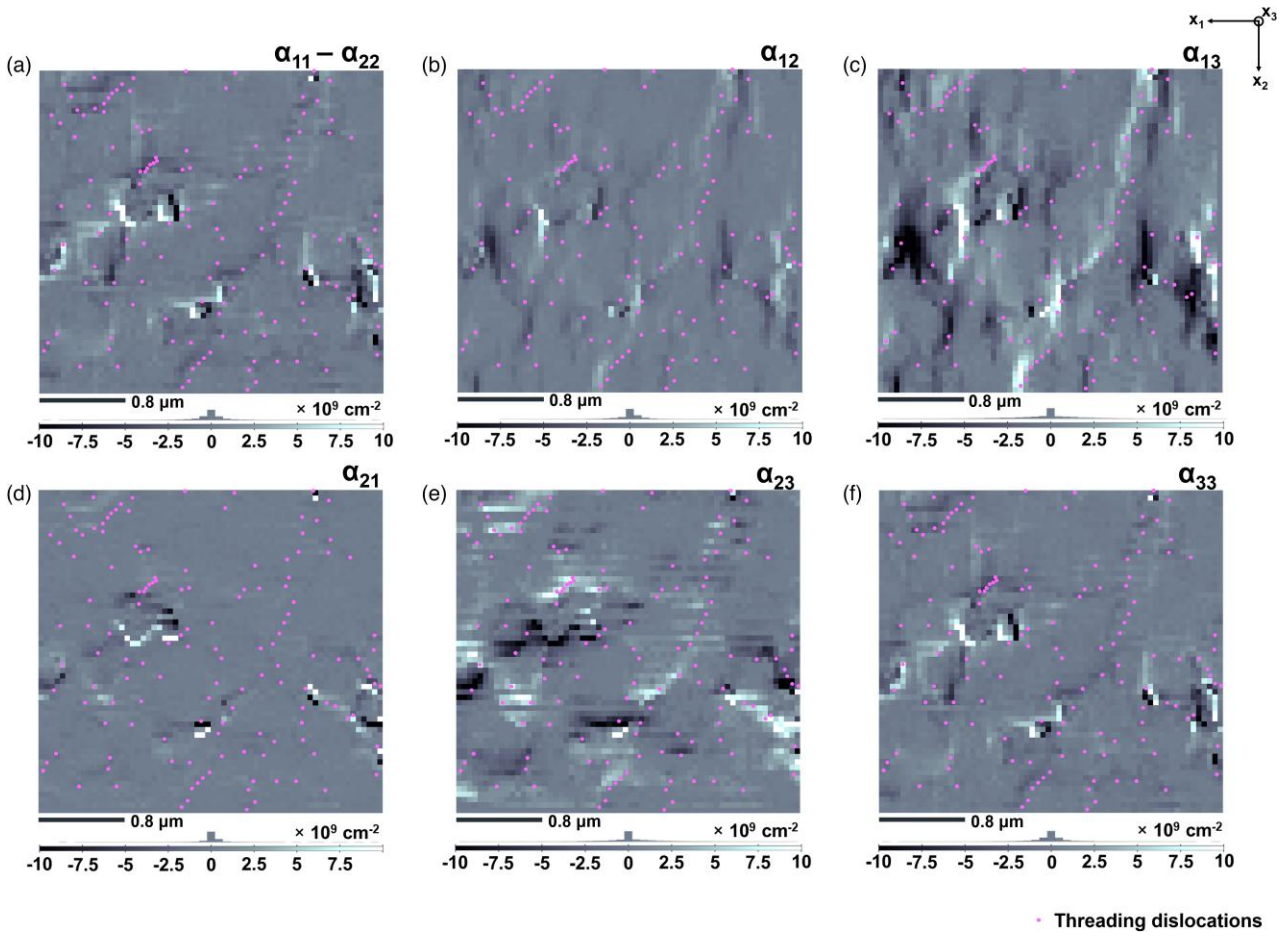

Fig. 5. The HR-EBSD maps showing one difference of terms and five known terms of the Nye tensor: (**a**) $\alpha_{11}-\alpha_{22}$, (**b**) α_{12} (edge), (**c**) α_{13} (edge), (**d**) α_{21} (edge), (**e**) α_{23} (edge), and (**f**) α_{33} (screw), with the sample reference frame shown. TDs are superimposed on the maps as pink dots.

characterizing the local Burgers vector of dislocation densities. Whereas the α_{12} and α_{21} components are computed by neglecting the contribution of the elastic strain, and the α_{31} and α_{32} components are not at all computable as the contribution of neither the lattice curvature nor the elastic strain is entirely assessable.

Figure 5a shows the difference of terms ($\alpha_{11}-\alpha_{22}$), and Figures 5b–5e show α_{12}, α_{13}, α_{21}, and α_{23} components of the Nye tensor, respectively, which correspond to the edge dislocations, while Figure 5f shows the α_{33} component denoting screw dislocation. The $\boldsymbol{b}$ values are considered as 3.190 and 5.189 Å for edge i.e., <a>-type and screw i.e., <c>-type components of Nye tensor, respectively (Schulz & Thiemann, 1977). We remind that the two numbers in the subscript represent the directions of the Burgers vector and dislocation line vector, respectively, in the sample reference system (shown in Fig. 5). Components corresponding to the edge dislocations with the line vector perpendicular to the observation surface (i.e., α_{i3} components) reveal larger values and wider distribution compared with the other components. This is anticipated as most of the dislocations with their line vectors are expected to be along the growth direction of the thin film. There will just be other smaller components (α_{12} and α_{21}) as the dislocation line is slightly inclined toward the x_2 and x_1 directions. In this context, a dislocation line vector inclined at a certain low angle with [0001] is considered to be perfectly aligned along [0001] for the density calculation in the present study. The average density of pure edge (i.e., α_{13} and α_{23}) dislocations ($\sim 1–2 \times 10^8$ cm^{-2}) is one order of magnitude higher than that of the pure screw (i.e., α_{33}) dislocations ($\sim 1.8 \times 10^7$ cm^{-2}). This finding is concordant with the previously reported values of the density of TD types in InAlN/SiC samples by HR-EBSD (Vilalta-Clemente et al., 2017). Especially, the regions where TDs form clusters show a higher density of edge dislocations, as recognized in Figures 5c and 5e. Specifically, zones 1 and 4 reveal the presence of both α_{13}- and α_{23}-type at higher density, while zones 2 and 3 divulge higher density of α_{23}- and α_{13}-type edge dislocations, respectively (Table 1).

Table 1. The Average Density of GNDs and the Dislocation Type (by the Components of Nye Tensor) of Different Zones That HR-EBSD Identifies for the Dislocation Clusters.

Zone Number	Avg. GND Density ($\times 10^9$ cm^{-2})	Dislocation Type
1	0.033	$\alpha_{13}+\alpha_{23}$ (edge)
2	4.6	α_{23} (edge)
3	0.031	α_{13} (edge)
4	1.5	$\alpha_{13}+\alpha_{23}$ (edge)

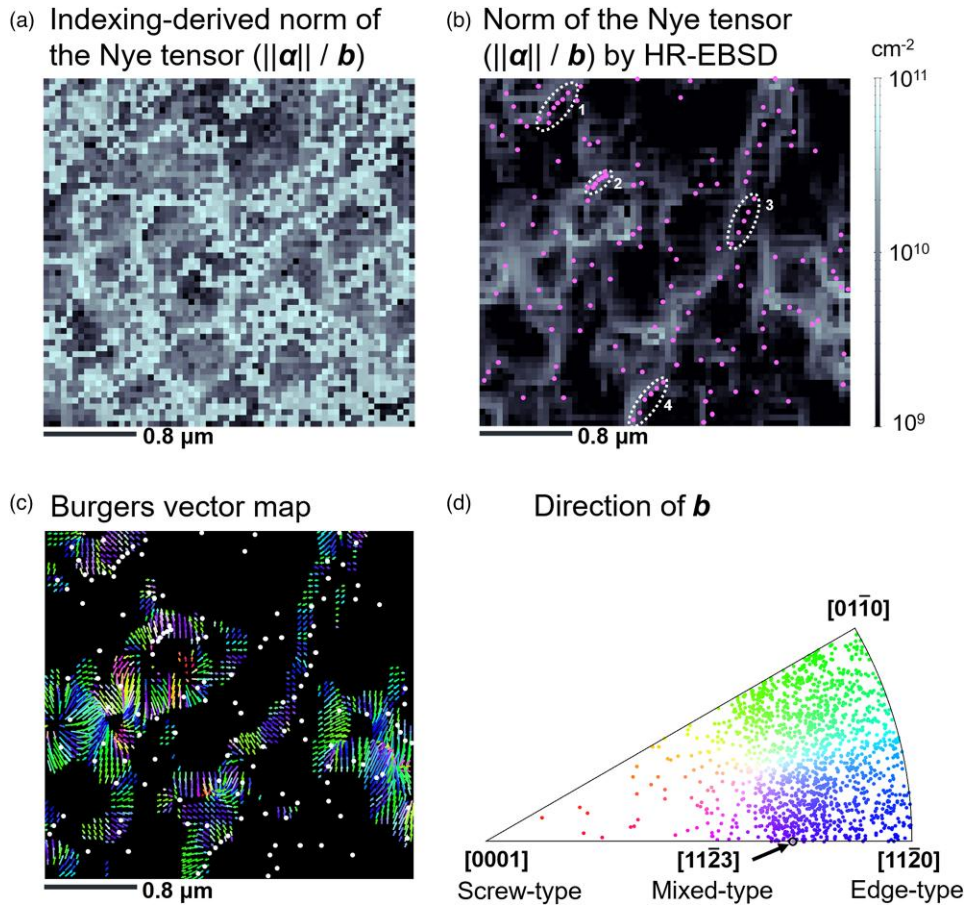

Fig. 6. The norm of the Nye tensor ($\|\boldsymbol{\alpha}\|/\boldsymbol{b}$) , i.e., geometrically necessary DD maps: (**a**) indexing-derived and (**b**) by HR-EBSD; (**c**) the Burgers vector map where the lengths of the arrows denote the magnitudes of ***b***, and (**d**) the IPF showing the direction of ***b***. The colors of the arrows within (**c**) are referred to as the *z*-IPF as shown in (**d**) where the perfect poles for edge, screw, and mixed dislocations are marked. The zones of dislocation clusters are shown by white ovals (dotted boundary) in (**b**), and TDs are denoted by pink and white dots in (**b**) and (**c**), respectively.

Entrywise Norm of Nye Tensor

The entrywise norm of the Nye tensor ($\|\boldsymbol{\alpha}\|$) is proportional to the bulk GND density in face-centered cubic material (El-Dasher et al., 2003). Equations (6) and (7) recapitulate this relation:

$$\|\boldsymbol{\alpha}\| = \sqrt{\alpha_{ij}\alpha_{ij}} \tag{6}$$

$$\rho_{\mathrm{GND}} \approx \frac{1}{b}\|\boldsymbol{\alpha}\| \tag{7}$$

HR-EBSD can provide distortion derivative components, which can give rise to the estimation of bulk DD for more complex lattice structures than the cubic ones by solving equation (7) (Ruggles & Fullwood, 2013). The norm of the Nye tensor as indexing-derived and HR-EBSD analyzed have been shown in Figures 6a and 6b, respectively, for the comparison between information provided by EBSD and HR-EBSD. Figures 6c and 6d display the Burgers vectors of the dislocations having the reference presented in Figure 6b. A disorientation angle <0.04° from the perfect [0001] orientation is neglected for the construction of this map. Since the density of edge-type GNDs is more when compared with that of the screw-type (Fig. 6d), the Burgers vector has been considered as lattice constant a (=3.190 Å) for the construction of the norm of Nye tensor (Schulz & Thiemann, 1977). Notably, the GND density is $\sim 10^9$ cm^{-2} from the analysis of the norm of the Nye tensor (plotted considering not only the α_{i3} components but all the known terms of the Nye tensor), which is the same order of magnitude as the TD density estimated from the ECC micrograph. Understandably, the regions with a high angle of in-plane rotation (Fig. 4) are surrounded by regions with a high density of GNDs. The values of average GND density are presented in Table 1 for those four regions, which show dislocation clusters (Fig. 2a). From the Burgers vector analysis, it can be established that the areas of high GND density are mostly constituted by pure edge dislocations with <a>-Burgers vector, i.e., $\frac{1}{3}[11\bar{2}0]$, $\frac{1}{3}[2\bar{1}\bar{1}0]$, and $\frac{1}{3}[\bar{1}2\bar{1}0]$, whereas, the screw i.e., <c>-type dislocations are very less in numbers. It is noteworthy that the average GND density in zones 2 and 4 is higher than that of the entire map as the GNDs are very closely spaced (i.e., within consecutive pixels) in those regions (Table 1). Generally speaking, the dislocations forming clusters are likely to be misidentified by HR-EBSD if the disorientation angle is considerably low. In this case, it is more an SSD density here, with no or negligible elastic rotation.

Residual Elastic Strain

The symmetric component of the displacement gradient tensor can be used to obtain the elastic residual strains, by the following equation (Asaro, 1979):

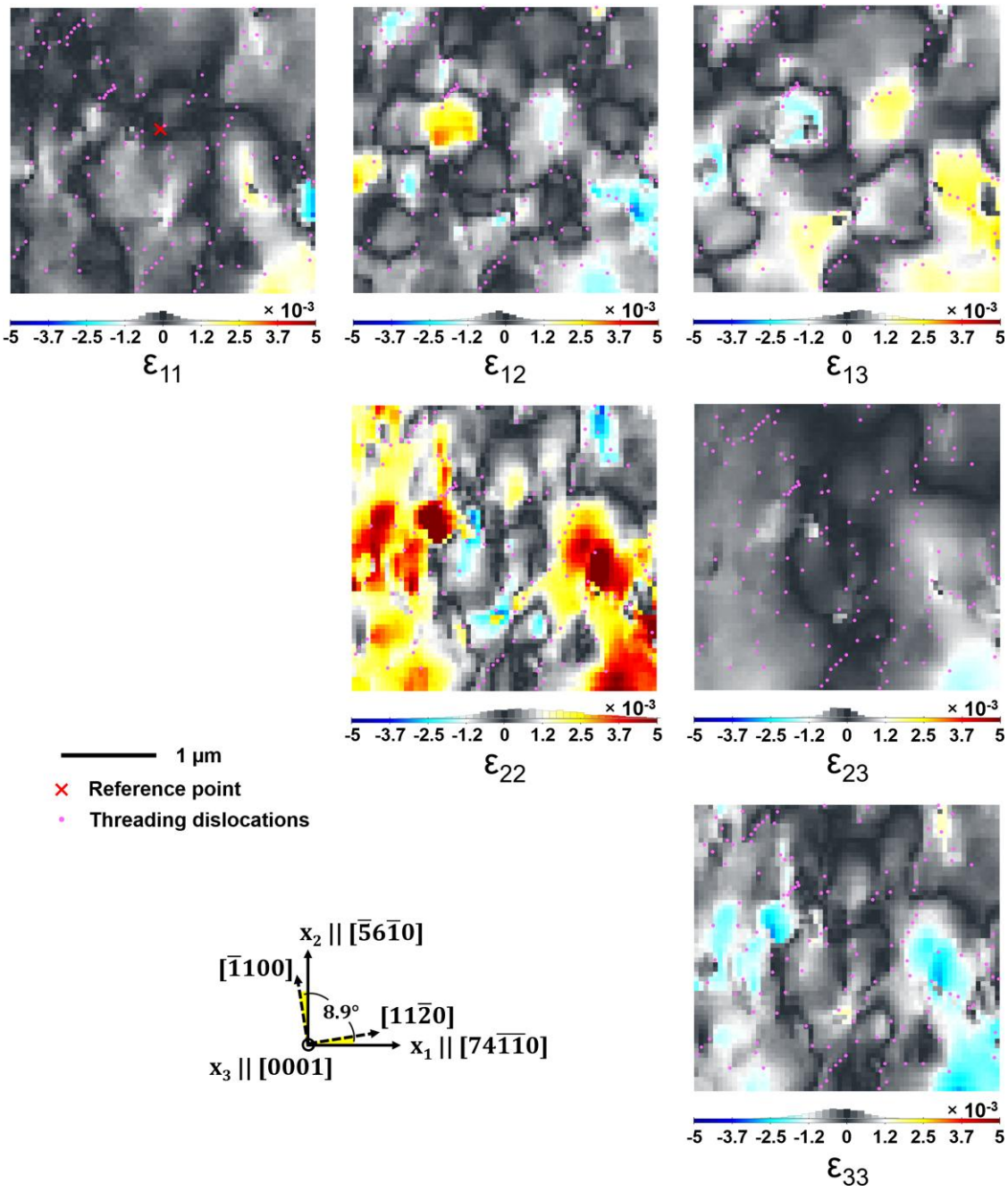

Fig. 7. Residual strain maps obtained from HR-EBSD. The red cross in ϵ_{11} is the user-chosen EBSP reference point, where the pixels with black, yellow/red, and cyan/blue colors correspond to areas with no strain, tensile strain, and compressive strain, respectively, along the [74$\bar{1}$$\bar{1}$0] direction. The sample reference axes are shown in the figure. TDs are superimposed on the maps as pink dots.

$$\varepsilon_{ij} = \frac{1}{2}\left(\frac{\partial u_i}{\partial x_j} + \frac{\partial u_j}{\partial x_i}\right) \tag{8}$$

A positive and a negative normal strains signify tensile and compressive strains, respectively. The normal and shear elastic strain maps are produced in Figure 7. The EBSP reference point is a user-chosen option, which is indicated by a red cross within ϵ_{11}, and elastic strain variations are calculated with respect to that point. It can be observed in all the maps that the areas showing tensile elastic strain (yellow) are necessarily adjacent to the areas with compressive elastic strain (cyan) and they are divided by a boundary with no strain (black). The higher strain variations are exhibited by the in-plane strain components, i.e., shear strain ϵ_{12} and normal strain ϵ_{22}. This can be attributed to the difference in thermal expansion coefficient and the lattice mismatch along the in-plane direction between the GaN layer and the substrate, which guides the formation of TDs (Vilalta-Clemente et al., 2017). Contrarily, the out-of-plane strain components, i.e., especially ϵ_{23} shear strain and ϵ_{33} normal strain, do not reveal much variation in the strain distribution, which is in accordance with the out-of-plane stresses to be close to zero to conform the biaxial strain of the GaN layer grown epitaxially. Given the EBSD step size (50 nm) and the quite large number of dislocations

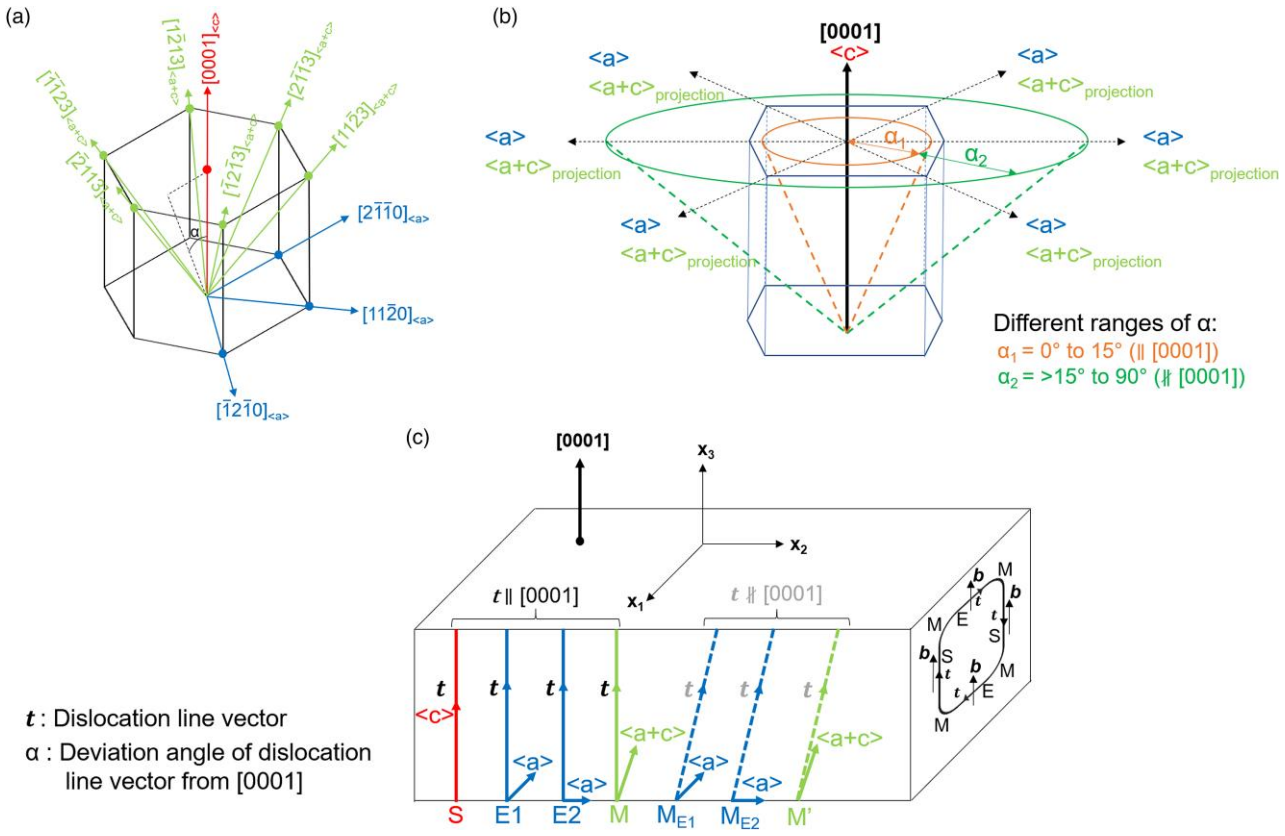

Fig. 8. Schematic illustration of (**a**) possible Burgers vectors (***b***) of edge (blue), screw (red), and mixed (green) TDs, (**b**) the consideration of dislocation line vectors (***t***) corresponding to the angle of deviation (α) from the [0001], and (**c**) different types of TDs with all possible dislocation lines and Burgers vectors and also a dislocation loop showing all possible line and Burgers vectors; *E*: edge (<a>-type), *S*: screw (<c>-type), *M*: mixed (<a + c>-type).

in our maps, it is not possible to identify elastic strain pattern characteristics of individual edge, screw, or mixed dislocations (Ernould et al., 2021). Furthermore, the estimation of TD density by HR-EBSD is supposed to be a lower bound as only the net Burgers vector is considered for the calculation. The input from some TDs is likely to have vanished ascribed to the cancellation of the vector sum of Burgers vectors.

Therefore, based upon the analysis of the norm and components of the Nye tensor, it can be concluded that the pure edge- or mixed-type dislocations with large edge component forming clusters are less likely to be distinguished by HR-EBSD even though the resolution is at such a level that each dislocation falls within an individual pixel. This can be attributed to their net small Burgers vector or small magnitude of individual Burgers vector (which is close to zero), resulting in minimal elastic strain and lattice rotation. Also in the case of ECCI, when a small tilt angle is used, the clusters of edge dislocations in a line appear as spatially smaller bright spots on the dark background than the TDs with a <c>-component, attributed to their smaller magnitude of Burgers vector when compared with the latter (Picard et al., 2009), as can be seen in Figure 1. This is unlike the results reported by Naresh-Kumar et al. (2012), where they observed no difference in the size of the black and white contrast for the edge and screw dislocations when a large tilt angle is used.

Synergy Between ECCI and HR-EBSD

The possible directions of Burgers vectors for edge, screw, and mixed dislocations are illustrated schematically in Figure 8a, with the color codes blue, red, and green, respectively. The dislocation line vector, i.e., ***t*** is considered as ∥ [0001] if the deviation α from the perfect [0001] is within 15° (α_1) and ⋕ [0001] if it is between 15 and 90° (α_2) (Fig. 8b), which is further considered for the construction of the grid map shown in Figure 9. The TD density of each type [i.e., edge, screw, mixed, and (edge + mixed)][2] is presented in Table 2 combining ECCI and HR-EBSD. The results are reported considering three different threshold angles of deviation of dislocation line vector from [0001], i.e., 10, 15, and 20°. Surprisingly, the line vectors of TDs are deviated from [0001] more often than not. Although, the dislocation lines are so far considered as ∥ [0001], they can be legitimately considered to have deviated from that direction since the directions of Burgers vector are not concentrated only at the edge (i.e., [11$\bar{2}$0]), screw (i.e., [0001]), or mixed (i.e., [11$\bar{2}$3]) poles but distributed throughout the inverse pole figure (IPF) (Fig. 6d). The combined ECCI + HR-EBSD method reveals the TDs with ***t*** ⋕ [0001] to be 89, 72, and 55% with the threshold angles 10, 15, and 20°, respectively (Table 2). The distribution of TDs, as identified by ECCI within the domain of interest, is plotted within the pixel-sized (as in HR-EBSD) grids according to their type (i.e., pure or mixed or combination), following the direction of Burgers vector analysis (Fig. 9). The deviation from the ideal <a>-Burgers vector for an edge, <c>-Burgers vector for a

[2] The (edge + mixed) dislocations are those <a>-type dislocations with inclined dislocation line vectors and having a large edge component, i.e. the angle between the dislocation line vector and the Burgers vector is close to 90°.

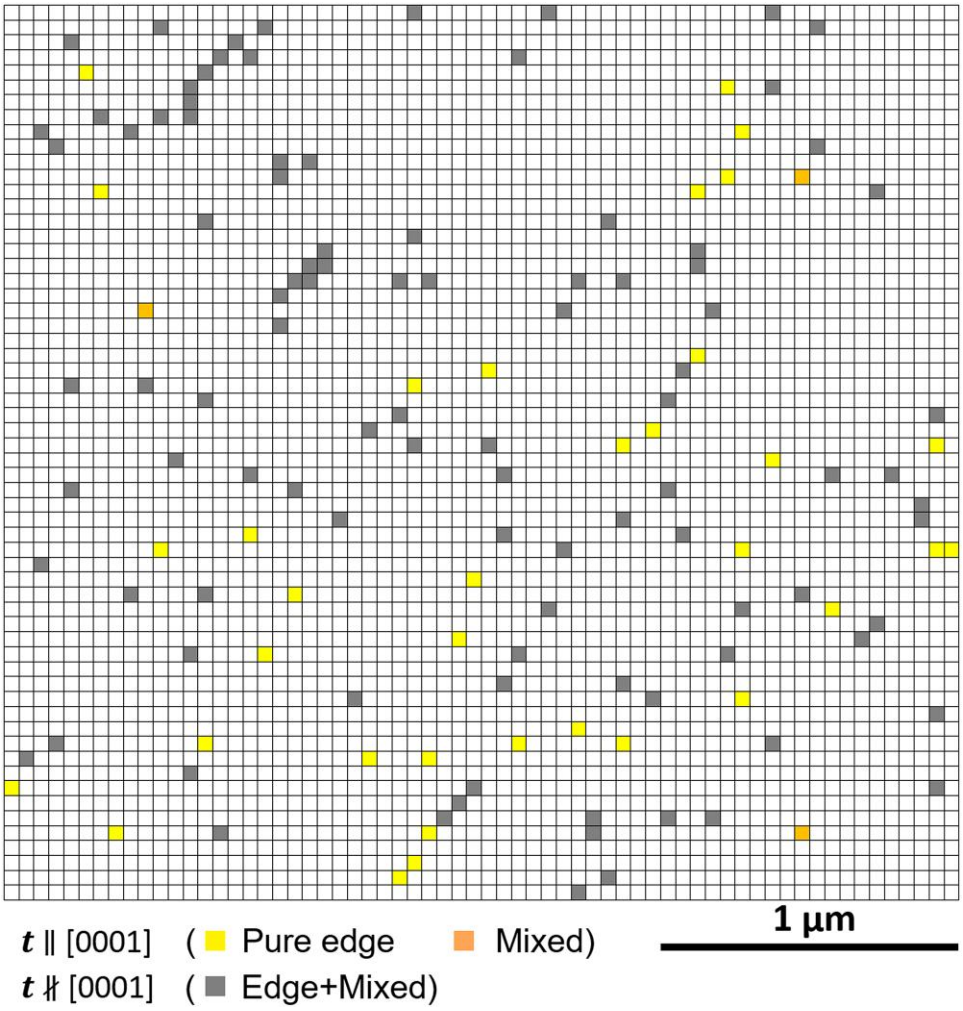

Fig. 9. The 60 × 64 grid (*l* × *w*) display of the area of interest where TDs are colored by their type following the direction of Burgers vector analysis using ECCI + HR-EBSD techniques. Within individual grids (i.e., pixel of HR-EBSD), pure edge, mixed, and (edge + mixed) dislocations are colored by yellow, orange, and gray, respectively. The threshold angle of deviation of $\boldsymbol{t}$ from [0001] is considered as 15°.

screw, and <a + c>-Burgers vector for a mixed is categorized as <15° for pure with $\boldsymbol{t} \parallel$ [0001] and between 15 and 90° for combined (or mixed with large edge component) with $\boldsymbol{t} \nparallel$ [0001]. Edge, mixed, and (edge + mixed) TDs are colored as yellow, orange, and gray, respectively, in Figure 9. For estimating the number of pure edge ($\boldsymbol{b} = 1\mathbf{a}$) and pure screw ($\boldsymbol{b} = 1\mathbf{c}$) types, a polar angle of deviation of <4° has been considered by Tsukakoshi et al. (2021) in a recent article, while for a mixed dislocation ($\boldsymbol{b} = 1\mathbf{a} + 1\mathbf{c}$) this angle is >4°.

As stated above, the ECCI method reveals most of the TDs as combined, i.e., (edge + mixed)-type (~72%), followed by edge-type (~25%), with very few mixed types and no screw type. This is in line with the findings by Wu et al. (1996) who showed that the edge character TDs represent a larger fraction in MOCVD films. It is noteworthy that the average deviation of the direction of Burgers vector of TDs from the perfect <c> (i.e., [0001]), perfect <a> (i.e., 1/3[$2\bar{1}\bar{1}0$], 1/3[$11\bar{2}0$], 1/3[$\bar{1}2\bar{1}0$], and their negatives), and perfect <a + c> (i.e., 1/3[$11\bar{2}3$], 1/3[$2\bar{1}\bar{1}3$], 1/3[$1\bar{2}13$], 1/3[$\bar{1}\bar{1}23$], 1/3[$\bar{2}113$], and 1/3[$\bar{1}2\bar{1}3$]) poles are 75.1 ± 11°, 48.7 ± 22.2° (with the lowest deviation of 38.9 ± 22.5° from 1/3[$11\bar{2}0$]), and 67.2 ± 14° (with the lowest deviation of 59.2 ± 15.8° from 1/3[$11\bar{2}3$]), respectively, as identified by combining ECCI and HR-EBSD (errors are the standard deviation from the average values). Therefore, it can be deduced for the present region of interest that most of the TDs are either (edge + mixed)-type (where $\boldsymbol{t} \nparallel$ [0001] and $\boldsymbol{b}$ far deviated from the screw component Burgers vector, i.e., exhibit negligible screw character) or edge-type (where $\boldsymbol{t} \parallel$ [0001]). Furthermore, the TDs that belong to the dislocation clusters are seen to be of pure edge-type (yellow) and (edge + mixed)-type (gray) TDs (Fig. 9). Figure 8c depicts the different types of TDs with all possible $\boldsymbol{t}$ and $\boldsymbol{b}$. The TDs with $\boldsymbol{t} \nparallel$ [0001] are mostly mixed-type TDs with an energetically favored inclined line direction (Mathis et al., 2001). From the Burgers vector analysis, it can be concluded that these inclined dislocations are (edge + mixed)-type (M_{E1} and M_{E2} in Fig. 8c) with negligible screw character. At a later stage of film growth, TDs participate in dislocation loop formation through their interaction which reduces the DD. These loops have a particular $\boldsymbol{b}$, however, depending on the $\boldsymbol{t}$ (which is mostly $\nparallel$ [0001]), the type can be edge, screw, or mixed, as shown schematically in Figure 8c. Nevertheless, following this approach, the proportion of edge- and mixed-type TDs cannot be explicitly determined for $\boldsymbol{t} \nparallel$ [0001].

The quality of the GaN crystalline film can be adversely affected by the formation of TDs; however, the effect is lesser when compared with other compound semiconductors

Table 2. Threading DD Measured by ECCI (Identification) and HR-EBSD (by Burgers Vector Analysis) Techniques Combined.

Method	Threshold Angle (From [0001])	Dislocation Line (t)	Type of TDs	TD Density ($\times 10^9$ cm^{-2})
ECCI + HR-EBSD	10°	∥ [0001]	Edge	0.125 ± 0.06
			Screw	—
			Mixed	0.02 ± 0.002
		⋕ [0001]	Edge + mixed	1.29 ± 0.09
	15°	∥ [0001]	Edge	0.365 ± 0.09
			Screw	—
			Mixed	0.02 ± 0.002
		⋕ [0001]	Edge + mixed	1.04 ± 0.1
	20°	∥ [0001]	Edge	0.59 ± 0.11
			Screw	—
			Mixed	0.031 ± 0.002
		⋕ [0001]	Edge + mixed	0.80 ± 0.1

(Bennett, 2010). It has been observed that the TDs with screw component Burgers vector i.e., mixed-type TDs are strong nonradiative centers when compared with the edge TDs, which are in majority in GaN thin films (Hino et al., 2000). The density of mixed-type TDs is higher in the nucleation layer; however, it is reduced substantially by the TD reaction resulting in the generation of edge-type TDs with the growth of the film (Moram et al., 2009). Although the material used in the present study contains the most number of edge- and (edge + mixed)-type TDs with an insignificant screw character, it necessitates suitable characterization to ensure practical applicability. The combination of ECCI and HR-EBSD (in the resolution limit of single dislocation) techniques has been proven to be effective in this regard. Notably, the current approach of using the HR-EBSD algorithm to acquire quantitative information about dislocation type bypasses the manual and meticulous $\mathbf{g}.\boldsymbol{b}$ calculation using ECC micrographs with multiple **g**-vectors.

Conclusion

To summarize, it has been observed that ECCI offers direct and fast imaging of dislocations, whereas HR-EBSD delivers quantitative information on the magnitude and direction of disorientations along with the character of the dislocations. Commonly, both of these nondestructive techniques are capable of analyzing large areas (comparatively less for HR-EBSD considering the time consumed to perform the experiment) on a bulk specimen in order to produce useful but complementary microstructural information. A large number of dislocations can be probed by both of these techniques, producing a statistically more significant result than a transmission electron microscope. Thin film GaN deposited on Si substrate exhibits the TDs of mostly (edge + mixed)-type with insignificant screw character. Although HR-EBSD provides information on elastic strain, lattice rotation, etc. quantitatively, to only count the number of TDs and estimate their density, ECCI is stand-alone. To image and count the dislocations (some are tiny faint spots without the black and white contrast), the ECC micrograph is preferred over HR-EBSD because of its smaller pixel size. The TDs forming clusters are mostly edge- and (edge + mixed)-type TDs. This is attributed to their small magnitude of individual Burgers vector or small net Burgers vector, resulting in minimal elastic strain as well as lattice rotation, which can be distinguished by methods that do not use channeling contrast for the identification of TDs. Nevertheless, following this approach, the proportion of edge- and mixed-type TDs cannot be explicitly determined for the dislocations with an inclined line vector ⋕ [0001]. In the present study, with the spatial resolution of 50 nm in HR-EBSD, it is not possible to identify elastic strain pattern characteristics or lattice rotations of individual dislocations that have been identified by the ECCI technique.

Availability of Data and Materials

Raw/processed data from this work are available upon demand.

Acknowledgments

The authors are thankful to the experimental facilities of MicroMat from LEM3 (Université de Lorraine—CNRS—ENSAM).

Financial Support

The authors gratefully acknowledge the European Union for the financial support provided through the AddMorePower project funding from the European Union's Horizon Europe research and innovation program under grant agreement No. 101091621. Views and opinions expressed are however those of the authors only and do not necessarily reflect those of the European Union. Neither the European Union nor the granting authority can be held responsible for them.

Conflict of Interest

The authors declare that they have no competing interest.

References

Amano H, Sawaki N, Akasaki I & Toyoda Y (1986). Metalorganic vapor phase epitaxial growth of a high quality GaN film using an AlN buffer layer. *Appl Phys Lett* **48**, 353–355. https://doi.org/10.1063/1.96549

Asaro RJ (1979). Geometrical effects in the inhomogeneous deformation of ductile single crystals. *Acta Metall* **27**, 445–453. https://doi.org/10.1016/0001-6160(79)90036-1

Ayers JD & Joy DC (1972). A crystallographic study of massive precipitates in Cu-Zn and Ag-Zn alloys utilizing selected area electron channelling. *Acta Metall* **20**, 1371–1379. https://doi.org/10.1016/0001-6160(72)90072-7

Beausir B & Fundenberger JJ (2017). Analysis Tools for Electron and X-ray diffraction. ATEX-software, www. atex-software.eu, Université de Lorraine-Metz, France, EU.

Bennett SE (2010). Dislocations and their reduction in GaN. *Mater Sci Technol* **26**, 1017–1028. https://doi.org/10.1179/026708310X12668415533685

Booker GR, Shaw AMB, Whelan MJ & Hirsch PB (1967). Some comments on the interpretation of the 'kikuchi-like reflection patterns' observed by scanning electron microscopy. *Philos Mag* **16**, 1185–1191. https://doi.org/10.1080/14786436708229969

Cardona A, Saalfeld S, Schindelin J, Arganda-Carreras I, Preibisch S, Longair M, Tomancak P, Hartenstein V & Douglas RJ (2012). TrakEM2 software for neural circuit reconstruction. *PLoS One* **7**, e38011. https://doi.org/10.1371/journal.pone.0038011

Chien FR, Ning XJ, Stemmer S, Pirouz P, Bremser MD & Davis RF (1996). Growth defects in GaN films on 6H–SiC substrates. *Appl Phys Lett* **68**, 2678–2680. https://doi.org/10.1063/1.116279

Choi Y-S, Park J-H, Kim S-S, Song H-J, Lee S-H, Jung J-J & Lee B-T (2004). Effects of dislocations on the luminescence of GaN/InGaN multi-quantum-well light-emitting-diode layers. *Mater Lett* **58**, 2614–2617. https://doi.org/10.1016/j.matlet.2004.03.021

Coates DG (1967). Kikuchi-like reflection patterns obtained with the scanning electron microscope. *Philos Mag* **16**, 1179–1184. https://doi.org/10.1080/14786436708229968

Dunlap BE, Ruggles TJ, Fullwood DT, Jackson B & Crimp MA (2018). Comparison of dislocation characterization by electron channeling contrast imaging and cross-correlation electron backscattered diffraction. *Ultramicroscopy* **184**, 125–133. https://doi.org/10.1016/j.ultramic.2017.08.017

El-Dasher BS, Adams BL & Rollett AD (2003). Viewpoint: Experimental recovery of geometrically necessary dislocation density in polycrystals. *Scr Mater* **48**, 141–145. https://doi.org/10.1016/S1359-6462(02)00340-8

Ernould C, Beausir B, Fundenberger J-J, Taupin V & Bouzy E (2021). Integrated correction of optical distortions for global HR-EBSD techniques. *Ultramicroscopy* **221**, 113158. https://doi.org/10.1016/j.ultramic.2020.113158

Forouzesh M, Sheng B & Liu Y-F (2020). 2020 Interleaved SCC-LCLC converter with TO-220 GaN HEMTs and accurate current sharing for wide operating range in data center application. In *2020 IEEE Applied Power Electronics Conference and Exposition (APEC)*, pp. 482–489. New Orleans, LA: IEEE. Available at https://ieeexplore.ieee.org/document/9124489/ (retrieved December 18, 2023).

Groon F, Pereira T, Beiranvand H, Schikowski S, Metschies D & Liserre M (2023). GaN-based multiport resonant converter for automotive applications. In *2023 IEEE Applied Power Electronics Conference and Exposition (APEC)*, pp. 892–899. Orlando, FL: IEEE. Available at https://ieeexplore.ieee.org/document/10131146/ (retrieved December 18, 2023).

Habiyaremye F, Guitton A, Chen X, Richeton T, Berbenni S, Schäfer F, Laplanche G & Maloufi N (2024). Influence of pre-existing configurations of dislocations on the initial pop-in load during nanoindentation in a CrCoNi medium-entropy alloy. *Philos Mag* **104**, 137–160. https://doi.org/10.1080/14786435.2023.2290541

Habiyaremye F, Guitton A, Schäfer F, Scholz F, Schneider M, Frenzel J, Laplanche G & Maloufi N (2021). Plasticity induced by nanoindentation in a CrCoNi medium-entropy alloy studied by accurate electron channeling contrast imaging revealing dislocation-low angle grain boundary interactions. *Mater Sci Eng A* **817**, 141364. https://doi.org/10.1016/j.msea.2021.141364

Hino T, Tomiya S, Miyajima T, Yanashima K, Hashimoto S & Ikeda M (2000). Characterization of threading dislocations in GaN epitaxial layers. *Appl Phys Lett* **76**, 3421–3423. https://doi.org/10.1063/1.126666

Jiang J, Britton TB & Wilkinson AJ (2013). Measurement of geometrically necessary dislocation density with high resolution electron backscatter diffraction: Effects of detector binning and step size. *Ultramicroscopy* **125**, 1–9. https://doi.org/10.1016/j.ultramic.2012.11.003

Kachi T (2018). Gan devices for automotive application and their challenges in adoption. In *2018 IEEE International Electron Devices Meeting (IEDM)*, pp. 19.5.1–19.5.4. San Francisco, CA: IEEE. Available at https://ieeexplore.ieee.org/document/8614563/ (retrieved December 18, 2023).

Kaminski N & Hilt O (2014). Sic and GaN devices—Wide bandgap is not all the same. *IET Circuits Devices Syst* **8**, 227–236. https://doi.org/10.1049/iet-cds.2013.0223

Kapolnek D, Wu XH, Heying B, Keller S, Keller BP, Mishra UK, DenBaars SP & Speck JS (1995). Structural evolution in epitaxial metalorganic chemical vapor deposition grown GaN films on sapphire. *Appl Phys Lett* **67**, 1541–1543. https://doi.org/10.1063/1.114486

Kikkawa T, Makiyama K, Ohki T, Kanamura M, Imanishi K, Hara N & Joshin K (2009). High performance and high reliability AlGaN/GaN HEMTs. *Phys Status Solidi A* **206**, 1135–1144. https://doi.org/10.1002/pssa.200880983

Kriaa H, Guitton A & Maloufi N (2017). Fundamental and experimental aspects of diffraction for characterizing dislocations by electron channeling contrast imaging in scanning electron microscope. *Sci Rep* **7**, 9742. https://doi.org/10.1038/s41598-017-09756-3

Kriaa H, Guitton A & Maloufi N (2019). Modeling dislocation contrasts obtained by accurate-electron channeling contrast imaging for characterizing deformation mechanisms in bulk materials. *Materials* **12**, 1587. https://doi.org/10.3390/ma12101587

Kriaa H, Guitton A & Maloufi N (2021). Modelling electron channeling contrast intensity of stacking fault and twin boundary using crystal thickness effect. *Materials* **14**, 1696. https://doi.org/10.3390/ma14071696

Kröner E (1959). Allgemeine kontinuumstheorie der versetzungen und eigenspannungen. *Arch Ration Mech Anal* **4**, 273–334. https://doi.org/10.1007/BF00281393

Kwong F, Li L, Ann S & Hass Z (2011). Gallium nitride: An overview of structural defects. In *Optoelectronics—Materials and Techniques*, Predeep, P (Ed.), pp. 99–136. School of Physics, Universiti Sains Malaysia, Malaysia: InTech, Available at http://www.intechopen.com/books/optoelectronics-materials-and-techniques/gallium-nitride-an-overview-of-structural-defects (retrieved December 19, 2023).

Lee K & Auh K (2001). Dislocation density of GaN grown by hydride vapor phase epitaxy. *MRS Internet J Nitride Semicond Res* **6**, e9. https://doi.org/10.1557/S1092578300000211

Mathis SK, Romanov AE, Chen LF, Beltz GE, Pompe W & Speck JS (2000). Modeling of threading dislocation reduction in growing GaN layers. *Phys Status Solidi A* **179**, 125–145. https://doi.org/10.1002/1521-396X(200005)179:1<125::AID-PSSA125>3.0.CO;2-2

Mathis SK, Romanov AE, Chen LF, Beltz GE, Pompe W & Speck JS (2001). Modeling of threading dislocation reduction in growing GaN layers. *J Cryst Growth* **231**, 371–390. https://doi.org/10.1016/S0022-0248(01)01468-3

Mishra M, Sharan J, Koul V, Kharbanda OP, Kumar A, Sharma A, Hackett TA, Sagar R, Kashyap MK & Gupta G (2023). Surface functionalization of gallium nitride for biomedical implant applications. *Appl Surf Sci* **612**, 155858. https://doi.org/10.1016/j.apsusc.2022.155858

Moram MA, Ghedia CS, Rao DVS, Barnard JS, Zhang Y, Kappers MJ & Humphreys CJ (2009). On the origin of threading dislocations in GaN films. *J Appl Phys* **106**, 073513. https://doi.org/10.1063/1.3225920

Narayanan V, Lorenz K, Kim W & Mahajan S (2001). Origins of threading dislocations in GaN epitaxial layers grown on sapphire by metalorganic chemical vapor deposition. *Appl Phys Lett* **78**, 1544–1546. https://doi.org/10.1063/1.1352699

Naresh-Kumar G, Edwards PR, Batten T, Nouf-Allehiani M, Vilalta-Clemente A, Wilkinson AJ, Le Boulbar E, Shields PA, Starosta B, Hourahine B, Martin RW & Trager-Cowan C (2022). Non-destructive imaging of residual strains in GaN and their effect on optical and electrical properties using correlative light–electron microscopy. *J Appl Phys* **131**, 075303. https://doi.org/10.1063/5.0080024

Naresh-Kumar G, Hourahine B, Edwards PR, Day AP, Winkelmann A, Wilkinson AJ, Parbrook PJ, England G & Trager-Cowan C (2012). Rapid nondestructive analysis of threading dislocations in wurtzite

materials using the scanning electron microscope. *Phys Rev Lett* **108**, 135503. https://doi.org/10.1103/PhysRevLett.108.135503

Nikandish R (2023). Gan integrated circuit power amplifiers: Developments and prospects. *IEEE J Microw* **3**, 441–452. https://doi.org/10.1109/JMW.2022.3221268

Nye JF (1953). Some geometrical relations in dislocated crystals. *Acta Metall* **1**, 153–162. https://doi.org/10.1016/0001-6160(53)90054-6

Ohno Y & Kuzuhara M (2001). Application of GaN-based heterojunction FETs for advanced wireless communication. *IEEE Trans Electron Devices* **48**, 517–523. https://doi.org/10.1109/16.906445

Pantleon W (2008). Resolving the geometrically necessary dislocation content by conventional electron backscattering diffraction. *Scr Mater* **58**, 994–997. https://doi.org/10.1016/j.scriptamat.2008.01.050

Pearton SJ (ed.) (2021). *GaN and Related Materials*, 1st ed. Boca Raton, FL: CRC Press.

Picard YN, Caldwell JD, Twigg ME, Eddy CR, Mastro MA, Henry RL, Holm RT, Neudeck PG, Trunek AJ & Powell JA (2007). Nondestructive analysis of threading dislocations in GaN by electron channeling contrast imaging. *Appl Phys Lett* **91**, 094106. https://doi.org/10.1063/1.2777151

Picard YN, Twigg ME, Caldwell JD, Eddy CR, Mastro MA & Holm RT (2009). Resolving the Burgers vector for individual GaN dislocations by electron channeling contrast imaging. *Scr Mater* **61**, 773–776. https://doi.org/10.1016/j.scriptamat.2009.06.021

Polian A, Grimsditch M & Grzegory I (1996). Elastic constants of gallium nitride. *J Appl Phys* **79**, 3343–3344. https://doi.org/10.1063/1.361236

Pushpakaran BN, Subburaj AS & Bayne SB (2020). Commercial GaN-based power electronic systems: A review. *J Electron Mater* **49**, 6247–6262. https://doi.org/10.1007/s11664-020-08397-z

Ruggles TJ, Deitz JI, Allerman AA, Carter CB & Michael JR (2021). Identification of star defects in gallium nitride with HREBSD and ECCI. *Microsc Microanal* **27**, 257–265. https://doi.org/10.1017/S143192762100009X

Ruggles TJ & Fullwood DT (2013). Estimations of bulk geometrically necessary dislocation density using high resolution EBSD. *Ultramicroscopy* **133**, 8–15. https://doi.org/10.1016/j.ultramic.2013.04.011

Runton DW, Trabert B, Shealy JB & Vetury R (2013). History of GaN: High-power RF gallium nitride (GaN) from infancy to manufacturable process and beyond. *IEEE Microw Mag* **14**, 82–93. https://doi.org/10.1109/MMM.2013.2240853

Schulz H & Thiemann KH (1977). Crystal structure refinement of AlN and GaN. *Solid State Commun* **23**, 815–819. https://doi.org/10.1016/0038-1098(77)90959-0

Smalc-Koziorowska J, Moneta J, Chatzopoulou P, Vasileiadis IG, Bazioti C, Prytz Ø, Belabbas I, Komninou P & Dimitrakopulos GP (2020). The heterogeneous nucleation of threading dislocations on partial dislocations in III-nitride epilayers. *Sci Rep* **10**, 17371. https://doi.org/10.1038/s41598-020-74030-y

Streit DC, Gutierrez-Aitken A, Wojtowicz M & Lai R (2005). The future of compound semiconductors for aerospace and defense applications. In *IEEE Compound Semiconductor Integrated Circuit Symposium*, 2005. CSIC '05, p. 4, Palm Springs, CA: IEEE. Available at http://ieeexplore.ieee.org/document/1531737/ (retrieved December 18, 2023).

Tanaka T, Ueda T & Ueda D (2010). Highly efficient GaN power transistors and integrated circuits with high breakdown voltages. In *2010 10th IEEE International Conference on Solid-State and Integrated Circuit Technology*, pp. 1315–1318. Shanghai, China: IEEE. Available at http://ieeexplore.ieee.org/document/5667650/ (retrieved December 19, 2023).

Tsukakoshi M, Tanikawa T, Yamada T, Imanishi M, Mori Y, Uemukai M & Katayama R (2021). Identification of Burgers vectors of threading dislocations in freestanding GaN substrates via multiphoton-excitation photoluminescence mapping. *Appl Phys Express* **14**, 055504. https://doi.org/10.35848/1882-0786/abf31b

Usami S, Ando Y, Tanaka A, Nagamatsu K, Deki M, Kushimoto M, Nitta S, Honda Y, Amano H, Sugawara Y, Yao Y-Z & Ishikawa Y (2018). Correlation between dislocations and leakage current of p-n diodes on a free-standing GaN substrate. *Appl Phys Lett* **112**, 182106. https://doi.org/10.1063/1.5024704

Vetury R, Zhang NQ, Keller S & Mishra UK (2001). The impact of surface states on the DC and RF characteristics of AlGaN/GaN HFETs. *IEEE Trans Electron Devices* **48**, 560–566. https://doi.org/10.1109/16.906451

Vilalta-Clemente A, Naresh-Kumar G, Nouf-Allehiani M, Gamarra P, Di Forte-Poisson MA, Trager-Cowan C & Wilkinson AJ (2017). Cross-correlation based high resolution electron backscatter diffraction and electron channelling contrast imaging for strain mapping and dislocation distributions in InAlN thin films. *Acta Mater* **125**, 125–135. https://doi.org/10.1016/j.actamat.2016.11.039

Vilalta-Clemente A, Naresh-Kumar G, Nouf-Allehiani M, Parbrook PJ, Boulbar EDL, Allsopp D, Shields PA, Trager-Cowan C & Wilkinson AJ (2015). High-Resolution electron backscatter diffraction in III-nitride semiconductors. *Microsc Microanal* **21**, 2217–2218. https://doi.org/10.1017/S1431927615011861

Voyiadjis GZ & Peters R (2010). Size effects in nanoindentation: An experimental and analytical study. *Acta Mech* **211**, 131–153. https://doi.org/10.1007/s00707-009-0222-z

Wang Y (2012). *Misfit Dislocation and Strain Relaxation at Large Lattice Mismatched III-V Semiconductor Interfaces*. Caen, France: Université de Caen. Available at https://theses.hal.science/tel-00779457 (retrieved May 21, 2024).

Wilkinson AJ, Meaden G & Dingley DJ (2006). High-resolution elastic strain measurement from electron backscatter diffraction patterns: New levels of sensitivity. *Ultramicroscopy* **106**, 307–313. https://doi.org/10.1016/j.ultramic.2005.10.001

Wilkinson AJ & Randman D (2010). Determination of elastic strain fields and geometrically necessary dislocation distributions near nanoindents using electron back scatter diffraction. *Philos Mag* **90**, 1159–1177. https://doi.org/10.1080/14786430903304145

Wu XH, Brown LM, Kapolnek D, Keller S, Keller B, DenBaars SP & Speck JS (1996). Defect structure of metal-organic chemical vapor deposition-grown epitaxial (0001) GaN/Al2O3. *J Appl Phys* **80**, 3228–3237. https://doi.org/10.1063/1.363264

Wu XH, Fini P, Tarsa EJ, Heying B, Keller S, Mishra UK, DenBaars SP & Speck JS (1998). Dislocation generation in GaN heteroepitaxy. *J Cryst Growth* **189–190**, 231–243. https://doi.org/10.1016/S0022-0248(98)00240-1

Xu Y, Xu G, An Z, Nielsen MH & Shen M (2023). Adversarial attacks and active defense on deep learning based identification of GaN power amplifiers under physical perturbation. *AEU Int J Electron Commun* **159**, 154478. https://doi.org/10.1016/j.aeue.2022.154478

Zaefferer S & Elhami N-N (2014). Theory and application of electron channelling contrast imaging under controlled diffraction conditions. *Acta Mater* **75**, 20–50. https://doi.org/10.1016/j.actamat.2014.04.018

Zhong Y, Zhang J, Wu S, Jia L, Yang X, Liu Y, Zhang Y & Sun Q (2022). A review on the GaN-on-Si power electronic devices. *Fundam Res* **2**, 462–475. https://doi.org/10.1016/j.fmre.2021.11.028

Zhu D, Wallis DJ & Humphreys CJ (2013). Prospects of III-nitride optoelectronics grown on Si. *Rep Prog Phys* **76**, 106501. https://doi.org/10.1088/0034-4885/76/10/106501